Materials Science in Semiconductor Processing 199 (2025) 109822

Contents lists available at ScienceDirect

Materials Science in Semiconductor Processing

journal homepage: www.elsevier.com/locate/mssp

Electrode variability and its impact on the characteristics of M@C_{80} molecular junctions (M = P, S, As, Se)

Anhar A. Oda [a], Alaa A. Al-Jobory [a], Sameer Nawaf [a,*], Nabeel F. Lattoofi [a], Moaaed Motlak [a], Ali Ismael [b]

[a] Department of Physics, College of Science, University of Anbar, Ramadi, Iraq
[b] Department of Physics, Lancaster University, Lancaster, LA1 4YB, UK

ARTICLE INFO

Keywords:
C_{80} molecular junctions
Transmission coefficient
Fullerene
Thermoelectric characteristics
Thermal conductivity

ABSTRACT

Consideration how electrons move through molecular junctions will enable researchers to create superior thermoelectric energy conversion materials. This research applies density functional theory (DFT) combined with the non-equilibrium Green's function (NEGF) formalism to study the electronic and thermoelectric behavior of metalloid-endohedral fullerenes (M@C_{80}, M = P, S, As, Se) connected to gold and graphene electrodes. The transmission coefficient T(E) undergoes significant changes when metalloids are introduced into C_{80}, which creates unique electronic transport characteristics. Metalloid-doped systems achieve notable improvements in thermoelectric response and performance metrics like the Seebeck coefficient (S) and figure of merit (ZT), especially when integrated with graphene electrodes. Se@C_{80} surpasses all other dopants in terms of thermal conductance and thermoelectric performance across both tested electrode types. Doping with metals is critical since it is important to change electronic transport properties and improve thermoelectric efficiency, which provides useful information for developing new molecular electronics and nanoscale energy conversion devices.

1. Introduction

Fullerene is a low-dimensional carbon nanostructure consisting of a number of spherically organized carbon atoms. Transistors [1], antioxidants [2], neurodegenerative disorder treatments [3], catalysts [4], quantum computing [5], photovoltaics [6], molecular diodes [7], nanomedicine [8], and biosensors [9] are just a few of the many uses for which its special qualities make it extremely important. The applicability of endohedral metallofullerenes is related to the fact that the corresponding metallic properties can be harnessed in the design of novel electronic devices. Organic supramolecular donor–acceptor (DA) conjugates often form the basic component in organic solar cells. The supramolecular are synthesized as molecular dyads, triads or even higher complexes. Typically, upon photoexcitation, an electron transfer occurs from a donor to an acceptor molecule. Besides enhancing charge separation, C_{60} is advantageous due to its low reorganization energy and three-dimensional charge mobility. Although various endohedral units have been used to synthesize these fullerenes, their limited stability and scarcity have constrained their application as electron acceptors in DA complexes [10]. The larger fullerene structure possesses the inherent property that the larger size of the cavity can lead to stability upon metal encapsulation. This is crucial in cases where larger metals are used to modify surface properties, which result from the increased charge-to-radius ratios. Previous studies suggest that larger metals generally lead to improved charge transfer properties with the molecular surface[11–13].

It is worth mentioning that the smaller diameter of C60 inhibits these beneficial interactions from happening by steric hindrance. C_{60} fullerenes are widely used for this property, but C80 fullerenes also can be used as an alternative. The enclosed metals have additionally a higher degree of freedom, because the C80 cage has an increased diameter. Although both C_{60} and C_{80} are fullerene molecules made up of only carbon atoms grouped in closed-cage structures, their sizes, symmetry, and characteristics are different. Buckminsterfullerene, or C_{60}, is a compound made up of 60 carbon atoms grouped in a soccer-ball-like truncated icosahedron with high symmetry. The structural complexity of C_{80}, on the other hand, is higher since it has 80 carbon atoms and can exist in multiple isomeric forms. C_{60} is more stable and has been researched more thoroughly because of its tiny size and great symmetry [14]. But because of its bigger internal cavity, C_{80} is better suited for

* Corresponding author.
E-mail address: Sameer@uoanbar.edu.iq (S. Nawaf).

https://doi.org/10.1016/j.mssp.2025.109822
Received 12 May 2025; Received in revised form 1 July 2025; Accepted 2 July 2025

endohedral doping, which traps metal atoms or clusters inside, increasing its potential for use in molecular electronics and nanotechnology. In terms of electronics, C_{80} might be more chemically reactive or conductive than C_{60} since it usually has a narrower HOMO–LUMO gap [15]. Applications like medication administration or catalysis may benefit from the increased contact with foreign atoms or molecules made possible by C_{80}'s higher surface area. All things considered, C_{80} is more stable and symmetrical, while C_{80} provides more adaptability and functional tunability for sophisticated material design. C_{80} can interact higher degrees with bigger molecules or metal atoms due to the greater number of carbon atoms, allowing it to be an optimal candidate for doping or functionalization. And, C_{80}'s larger size increases its compatibility with certain applications, like solar cells or molecular electronics, where geometry and size are vital to the efficiency. C_{80} with its modified electronic distribution and extended surface area help increase charge transport efficiency and stability of composite materials.

In order to address the metal atom quantization and its effect on the magnetic properties, the so-called metal endohedral fullerenes were proposed: metal atoms or clusters are encapsulated in fullerene cages like (C_{60}, C_{80}, etc.). The interaction between the metal center and the carbon cage endows these compounds with unique properties. All kinds of endohedral fullerenes are also referred to as metal@fullerenes complexes, with the endohedral metal atoms filling the fullerene cage usually being 3d or 4d transition metals TM or lanthanide elements because of appropriate sizes, electronic structures, and bonding abilities for encapsulation in carbon fullerene cages. 3d elements (transition metal (TM)) such as Scandium (Sc), Titanium (Ti), Vanadium (V), Iron (Fe) and 4d elements (TM) such as Yttrium (Y), Zirconium (Zr), Molybdenum (Mo) in addition to lanthanides Lanthanum (La), Cerium (Ce), Gadolinium (Gd) and Ytterbium (Yb) have atomic and ionic radii close to the radius of vessel closed within fullerenes. Medium and larger metals or atoms like Cesium (Cs) and Barium (Ba) have the ability to distort the fullerene cage, while even small atoms like Lithium (Li) and Beryllium (Be) can interact too weakly with the cage. This observation can be majorly attributed to the electrostatic (e.g. van der Waals) interactions between the fullerene cage and not the overall d-electron density of both transition metals and lanthanides, with the experimental observation indicating that fully filled d-orbitals of the transition metals and lanthanide can interact strongly with carbon cages. Moreover, these metals tend to have d or f orbitals that are only partially filled, making room to bond with the π-system of the fullerene. They donate or accept electrons, which results in stable oxidation states that preserve charge neutrality in the cage. The performance of molecular junctions is largely determined by spin and phonon dynamics in addition to electronic charge transport, as recent studies into molecular-scale devices have shown. For example, research on organic molecule based molecular junctions has demonstrated that the coupling between the molecule and electrodes has a significant impact on the production of pure spin currents and effective phonon thermoelectric transport [16,17]. It is clear from comparing this to spin and phonon transport in organic molecule systems that choosing the right electrode is not only essential for maximizing charge transport but can also be used to engineer multifunctional behavior in fullerene-based junctions, such as spin-filtering and thermoelectric effects.

Due to their high stability and favorable energetics, transition metal endohedral fullerenes are an important focus of current experimental and theoretical work. Recently, extensive research has focused on large endohedral fullerenes containing small clusters, owing to their distinctive structures and properties. *Caliskan S.* employs DFT and the Non-Equilibrium Green's Function Formalism to explore the spin-dependent electronic characteristics of $X@C_{70}$ (X = N, B) fullerene molecules [18]. The results indicate that the Au-B@C_{70}-Au device displays a nonlinear response to an applied bias ranging from −1 V to 1 V, independent of spin orientation. *Oda A. and Al-jobory A.* investigated the effect of electrode type on electric and thermoelectric properties of $M@C_{60}$ [19]. They showed that the electrical conductivity of gold electrodes is greater than that of graphene electrodes, whereas the Seebeck coefficient (S) is higher in graphene than in gold. *N. Maloufi* et al. utilized DFT within periodic boundary conditions (PBCs) to study the structural and electrical properties of neutral and charged $M@C_{60}$ systems [20]. Their structural analysis indicates that the geometry of endohedral fullerenes deviates from an ideal spherical shape. *S. Sarfaraz* et al. explored the hydrogen evolution reaction in C_{60} fullerenes doped with single atoms of ten different metals, including Sc, Ti, V, Cr, Mn, Fe, Co, Ni, Cu, and Zn [21]. The findings indicated that the $Fe@C_{60}$ complex exhibits the greatest catalytic activity in the hydrogen evolution process. *Sergeyev D.* employed density functional theory simulations to study the transport properties of a single-electron transistor (SET) based on metallofullerenes $Me@C_{60}$ (where Me represents Li, Na, and K) [22]. The results show that the energy of a negatively charged metallofullerene is lower compared to a neutral metallofullerene.

In this work, we study the electronic properties of the $M@C_{80}$ molecular junctions with M = P, S, As and Se on gold and graphene electrodes. This study seeks to demonstrate how doping and the type of electrode can link together and influence electronic transport. Group 15 (P, As) and Group 16 (S, Se) elements impart distinctive electronic features within the C_{80} cage. The contribution of the p-orbital of P and As in the π-electron cloud of the fullerene contributes to conductivity [23,24] Sulfur (S) and Selenium (Se) possess lone pairs influencing charge transfer and electrode interaction. These elements can also affect quantum interference effects in and electron transmission across the junction in the presence of these elements inside the C_{80}. They are useful for molecular electronic devices, as they can produce n-type or p-type behavior depending on the type of electrode (gold or graphene).

1.1. Computational details

Electronic structure calculations were performed using the DFT code SIESTA [25]. The GGA-PBE (Generalized Gradient Approximation – Perdew, Burke, and Ernzerhof) exchange-correlation functional is used in the computations. The optimal geometry of the C_{80} cage with the endohedral metal ions was determined by exploring various atomic configurations to identify the lowest energy structure. In each case, the molecule was relaxed until all the forces on the atoms were less than 0.04 V/Ang. SIESTA employs pseudo-atomic orbitals, and the relaxation was carried out using a double-zeta plus polarization orbital basis set. Norm-conserving pseudopotentials were employed, with a real-space grid defined by an energy cutoff of 200 Ry. To calculate electron transport, the molecule was connected to gold and graphene electrodes as shown in Fig. 1. Due to the large contact area of the C_{80} cage, a 5x5 atom layer of (111) gold was used to represent the electrode surface. The gold electrode bulk structure consists of 125 atoms arranged in a well-ordered configuration. It has overall dimensions of 12.96 Å × 10.00 Å × 10.64 Å in the x, y, and z directions, respectively. It contains five atomic layers each with 25 Au atoms. The layers are ranged at (z = 0.00, z = 2.66, z = 5.32, z = 7.98, and z = 10.64) Å with order to keep as close to ideal stacking as possible. The atomic structure has a face-centered cubic (FCC) arrangement, indicative of the crystalline structure for Au. [26,27]. The atoms are closely packed, maintaining a high coordination number that enhances structural stability. Due to the periodicity of the layers, the surface would have minimal reconstruction and is key to maintaining its electronic properties. Furthermore, the smooth and ordered surface of the electrode allows for predictable interfacial interactions with adsorbates or nanomaterials, ideal for electronic and catalytic applications [28,29]. The optimum binding location was found by calculating the binding energy as a function of the separation distance *z*, considering basis set error corrections. The graphene electrode bulk structure consists of 240 carbon atoms arranged in 23 layers. All layers contain 10 atoms and some layers contain only a couple of atoms because they are likely hitting a surface termination or edge effect. The layers have reasonable spacing along the z-dimension at

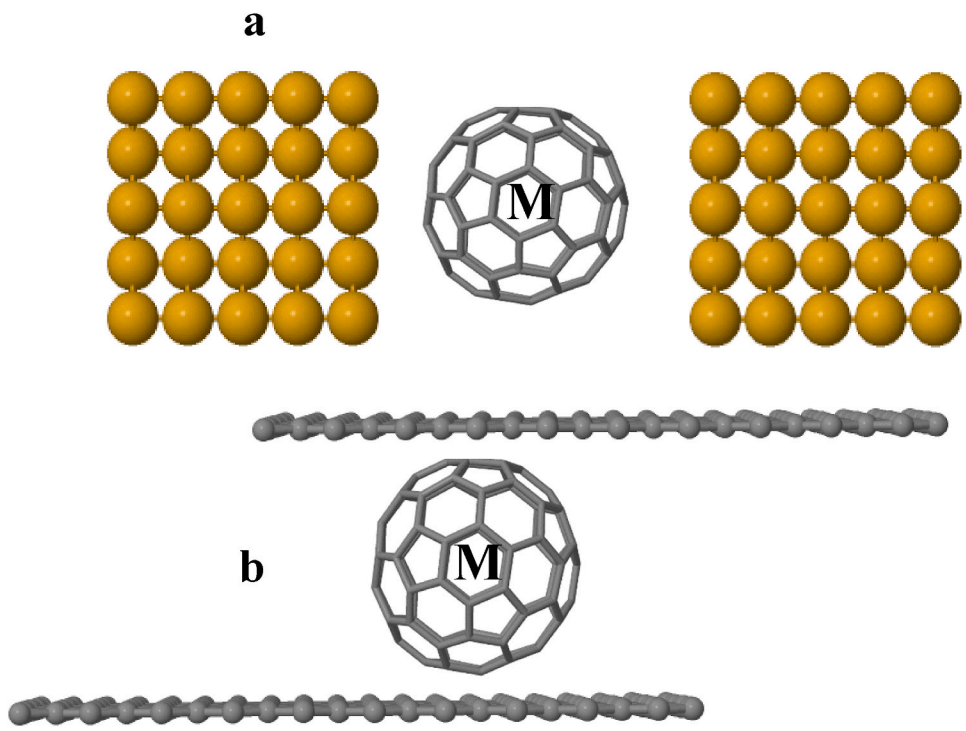

Fig. 1. (a) The structure of M@C_{80} connecting the gold electrode, (b) the structure of M@C_{80} connecting the Gr electrode

an interval from 0.00 Å – 28.02 Å. The total structure size is 0.00 Å × 19.88 Å × 28.02 Å, in the x, y, and z directions, respectively. In terms of structural properties, the graphene layers reflect the honeycomb lattice arrangement typical of carbon atom hexagons with strong covalent bonds in the plane. The layers in graphene are layered for superior electrical conductivity and mechanical flexibility [30]. The consistency of the interlayer spacing is very important for sustained electronic properties and for facilitating charge transport. These structural details are part of considering the range of properties exhibited by graphene electrodes in the contexts of nanoelectronics and energy storage applications. From a structural position, this orientation is of great importance in nanoelectronics, sensing applications, and energy storage devices where charge transfer and stability are core considerations. The effect of cage size and geometry on dopant behavior and electronic structure must be considered in order to clarify the structural and electronic benefits of C_{80} over C_{60}. The production of curvature-induced electronic localization states, which are frequently seen in smaller fullerenes, is lessened by the bigger cavity of C_{80} (~8.2 Å compared to ~7.1 Å in C_{60}). This facilitates improved electronic delocalization and a more even distribution of π-electron density, both of which are beneficial for charge transfer. Furthermore, C_{80} provides more internal volume and spatial flexibility, which lessens steric obstruction when metalloid dopants are present. The doped system's structural stability is aided by the C_{80} framework's increased rigidity. The electron transport is calculated along the device's longitudinal axis (z-direction) for all junctions in this study. The armchair orientation of the graphene sheet with 96 carbon atoms is used as a graphene electrode.

The M@C_{80} structure with gold and graphene electrodes can be analyzed using nonequilibrium Green's function (NEGF) theory implemented in the GOLLUM package [31]to determine its electronic and thermoelectric properties. This approach allows for the calculation of the transmission coefficient T(E), the electrical conductance $\log\left(G/G_0\right)$, the Seebeck coefficient S, the thermoelectric figure of merit ZT, and the thermal conductance K. The transmission coefficient T(E) provides insight into the probability of electron transmission across the M@C_{80} junction, revealing quantum transport behavior and energy-dependent conduction channels. It is obtained from the Green's function and self-energies of the electrodes. The electrical conductance G is calculated using the Landauer formula:

$$G = G_o \int_{-\infty}^{\infty} T(E)\left(-\frac{\partial f}{\partial E}\right) dE \quad (1)$$

Where $G_o = \frac{2e^2}{h}$ is the conductance quantum, and $\left(-\frac{\partial f}{\partial E}\right)$ is the Fermi-Dirac distribution.

The Seebeck coefficient S, also known as the thermopower, measures the voltage generated in response to a temperature gradient and is calculated as:

$$S(E) = -\frac{1}{eT}\frac{L_1}{L_o} \quad (2)$$

$$\text{Where } L_i = \int_{-\infty}^{\infty} dEp(E)(E - E_F)^i \quad (3)$$

The integral is obtained L_0, L_1, L_2 at $i = 0, 1, 2$ respectively.

The thermoelectric figure of merit ZT determines the efficiency of the material for energy conversion and is defined as:

$$ZT = \frac{GS^2}{\kappa_e} T \quad (4)$$

Here G, and κ both represent electrical and thermal conductance, respectively, T denotes the ambient temperature, and S refers to the Seebeck coefficient.

Since ZT represents the material's capacity to produce electrical power from a specific thermal gradient, it is clear from this relationship that an increase in power factor (GS^2) results in an improvement in ZT. Conversely, a larger κ_e lowers ZT because it promotes heat transfer and reduces the temperature differential across the device, which lowers thermoelectric efficiency. Thus, attaining a high ZT necessitates striking a precise balance between minimizing thermal losses and optimizing electrical transport characteristics.

The electronic thermal conductance κ_e are given by the following equation:

$$\kappa_e = \frac{2}{h}\int_{-\infty}^{\infty}(E-E_f)^2 T(E)\left(-\frac{\partial f}{\partial E}\right)dE \quad (5)$$

2. Results and discussion

In molecular junctions such as M@C_{80} (where M = P, S, As, Se), charge state and electron localization are significant contributing factors towards assessing the electronic transport properties of the system. The charge density maps can show how charge from the endohedral atom in the molecular junction is residing in the fullerene cage and which will result in electronic tunneling. Charge tendency for the fullerenes results from the charge density of electronegative elements such as S and Se, which typically attract greater charge, leading to more localized electronic states. The electron localization function (ELF) tells us to what degree charge is delocalized within the system. For example, a high ELF value near the metal center shows strong electron confinement of charge within the junction, and the behavior of tunneling characteristics in transport experiments is affected by this. Conversely, a more delocalized ELF distribution enhances charge transfer between the molecule and electrodes. The interaction with gold or graphene electrodes further modifies the charge density, impacting the junction's rectification and conductance properties. Fig. 2 demonstrates the charge density distribution with a contour plot for a C_{80} molecule. The contour plot shows that the charge density is high around each of the labelled "C" atoms, with contour lines closely spaced around the carbon nuclei. The charge density is highest at the atomic centers, then decreases outward, denoting the spatial distribution of the electrons surrounding the atoms. The symmetry of the charge density arrangement is representative of the nearly spherical structure for C_{80} fullerenes. The charge density is lower between atoms, as indicated by the more spread contours which signify the region of lower electron density in covalent bonding.

Fig. 3 demonstrates the Electron Localization Function (ELF) of a C_{80} fullerene. In the 3D plot, locations of high ELF values are peaks and warm colors (red and yellow), suggesting electron localization like that experienced in bonds and lone pairs. Low ELF values are represented in flat surfaces and cool colors (blue and green), suggesting low electron localization, typically analogously to delocalized or non-bonding electron densities. The high peaks illustrated in the plot around each carbon atom illustrate the strong covalent bonding network associated with fullerene materials. ELF values near 1 illustrate nearly perfect localization (strong covalent bonding). ELF values near 0.5 illustrate the presence of delocalized electron density. The bonding framework in C_{80}

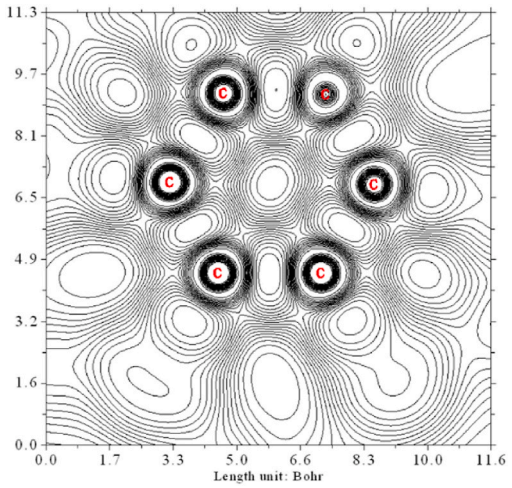

Fig. 2. The charge density distribution with a contour plot for a C_{80} molecule.

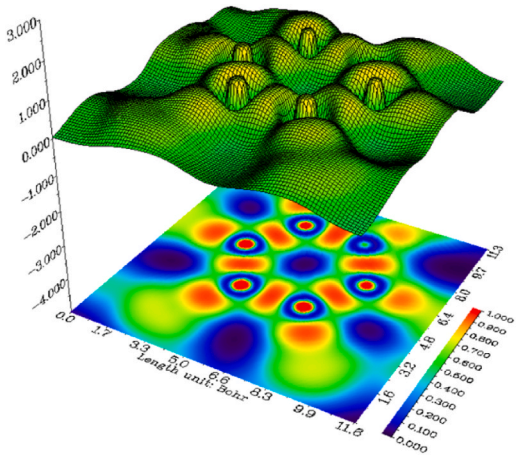

Fig. 3. The Electron Localization Function (ELF) of a C_{80} fullerene.

remains with substantial features of localized bonding but also fingerprinted with some delocalization in fullerenes, likely limiting the spatial integrity required for stability and special electronic characteristics.

The charge density and ELF of C_{80}, P@C_{80}, S@C_{80}, As@C_{80}, respectively are represented in Fig. S1 and S2 in the SI file. The central dopant atom (P, S, or As) in each plot is surrounded by carbon atoms, and the filled contour lines represent areas of high electron density (i.e., rich region of electronic charge). The charge density is most contained around phosphorus in P@C_{80}, indicating that there is strong interaction with the carbon cage surrounding it as shown in Figure S1 (a). In S@C_{80} as shown in Fig. S1(b), there is higher electron delocalization since the charge density is more diffuse, implying the bonding must be somewhat weaker. The contour lines in As@C_{80} (Fig. S1(c)) have a wider spacing than in P@C_{80}, but are narrower compared to S@C_{80}. Thus As@C_{80} falls in between P@C_{80} and S@C_{80} with respect to localization. Each of the configurations show symmetry distortions about the dopant which influence the underlying electron distribution and can have specific consequences for stability and electronic characteristics of the fullerene alone. However, the regions of highest electronic density as expected are found concentrated around the carbon atoms, and thus the fullerene cage should remain intact. The ELF displays slightly less localization for S@C_{80} (Fig. S2(b)) than for P@C_{80}(Fig. S2(a)), signifying that sulfur interacts with the C_{80} cage less strongly due to its higher electronegativity and distinct bonding preferences. As@C_{80} as in Fig. S2(c), shows a more delocalized ELF pattern than both P@C_{80} and S@C_{80}, showing that arsenic interacts with the carbon framework in a weaker manner. The structure of the ELF surfaces supports these results, showing that P@C_{80} displays sharper features than S@C_{80} and As@C_{80}. The shift in ELF patterns shows how the size, electronegativity, and electronic configuration of the dopant atom affect the electron distribution inside the fullerene. As@C_{80} appears to preserve wider electron sharing, which could improve overall stability by promoting more delocalized bonding. Less covalent character in the interaction with the cage is suggested by the comparatively flatter ELF profile of S@C_{80}. The charge density distribution and the electron localization function (ELF) plots were analyzed using Multiwfn program [32,33].

The ground state of the isolated Group V atoms is 4S, while the fullerene ground state is a totally symmetric singlet. The expected electronic ground state for the endohedral complex is also a quartet. In order to study the electrical and thermoelectric properties of M@C_{80}, we need to determine the fundamental quantum transfer coefficient T(E), which describes the probability of transfer T(E) of electrons with energy E passing through fullerene from left-sided gold or graphene electrodes to right-sided ones (Fig. 4).

The DFT-calculated Fermi level, which is a reference point for examining transport properties, is shown by the vertical dashed line.

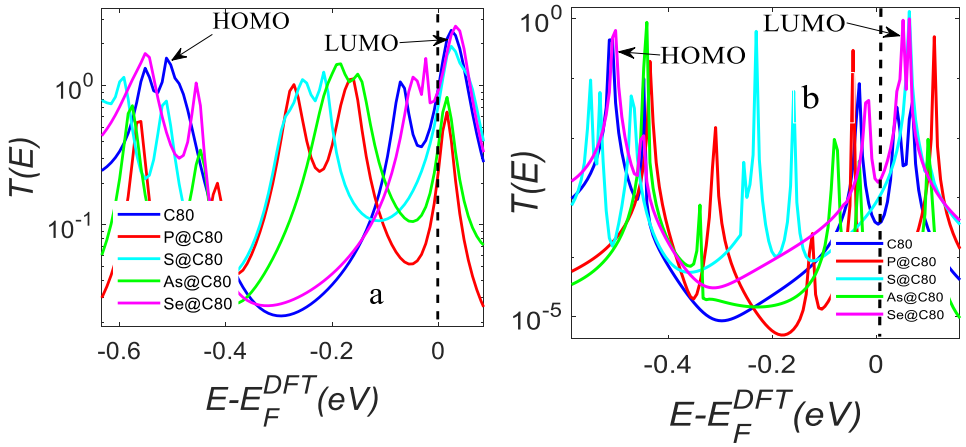

Fig. 4. The transmission coefficients (T(E)) for metalloid-doped C_{80} systems ($P@C_{80}$, $S@C_{80}$, $As@C_{80}$, and $Se@C_{80}$) connected to gold (Au) and graphene (Gr) electrodes.

Resonant states that play a major role in electronic transport are indicated by peaks in the transmission spectrum close to $E\text{-}E_F = 0$. The possibility of carrier tunneling or hopping rises when these peaks closely match E_F, improving electrical conductivity. The lowest unoccupied molecular orbital (LUMO) and the highest occupied molecular orbital (HOMO) are two examples of frontier molecular orbitals that frequently correlate to these peaks. Because of their increased charge carrier selectivity, systems with well-positioned and sharp peaks around E_F typically have better thermoelectric performance and favorable transport properties. Furthermore, the effect of metalloid doping on the electronic structure and the intensity of the coupling between the molecule and the electrodes is reflected in the shift of transmission peaks with respect to E_F. The effects of various dopants and electrode types are reflected in the changes in these orbital energies. However, not all barrier orbital energies correlate to high transmission peaks, as can be shown in the transmission spectra, especially when these orbitals have a poor coupling to the electrodes. This implies that rather than being driven only by HOMO and LUMO levels, transport is frequently dominated by molecular states that are more highly hybridized and more aligned with the electrode states.

T(E) transmission coefficients for systems metalloid doped C_{80} are shown in Fig. 4, where their metalloid transport behavior with respect to gold (Au) and graphene (Gr) electrodes is illustrated. Fig. 4ul. The transmission coefficients for Au electrodes show strong electronic transport with multiple resonant peaks, which are clearly indicative of strong Au electrodes. Undoped C80 is used as a benchmark and to understand the changes in transport properties when doped with P, S, As and Se. P doped system shows high transmission on certain energy ranges. At the same time, S and As-doped systems show specific energy ranges with low levels of transmission, suggesting the presence of a localized state which hinders transport. In Fig. 4b comes the same doped systems appear but with Gr electrodes, where the overall transmission is lower for some ranges, especially for the lower energies. The occurrence of anti-resonance effects, which can impede the flow of electrons, may be responsible for the sharp peaks detected in transmission for some dopants. [34]. Evaluating both scenarios, it can be observed that the gold electrode system, in general, exhibits greater transmission as compared to the graphene electrode system, which shows additional scattering effects. This demonstrates how the choice of electrode material affects the charge transport characteristics of C_{80} significantly. The highest transmission peak is associated with the home orbiting when it is below the Fermi level, and the lowest peak above it corresponds to the lowest unoccupied molecular orbital. Energy gap between these peaks is defined as the separation of high orbiting missiles and low orbiting missiles, which is altered depending on the type of dopant. In Fig. 4a each and every dopant displays distinct shifts of each homo and lumo position. $Se@C_{80}$ has a wider gap compared to $P@C_{80}$, indicating lower conductivity and hence a higher gap. In Fig. 4b graphene electrodes are shown to change lumo and homo orbital positions which yields different results for transmission compared to gold. The changes in homo and lumo positions demonstrates how changing charge of C80 has great impacts on its structure, and thus can be used in molecular electronics.

Figure (5) shows the dependence of the conductance log (G/G_0(for C80 metalloid-doped systems on the energy, bringing out the Fermi level. Systems connected to Au electrodes are shown in Fig. 5a, whereas Fig. 5b represents systems connected to Gr electrodes. Together with the undoped C80 as a reference, P, S, As and Se doping were performed to observe the effect on conductance. Slicing the above information into conductance spectra, multiple peaks are recorded owing to energy changes in the electron transport system. Overall conductance for the P-doped system with Au electrodes also showcased positive results within certain energy areas [35]. Values of electrical conductivities shown in 5a are observed to be for $P@C_{80}$, $S@C_{80}$, $As@C_{80}$, $Se@C_{80}$: −0.72, −0.1, −0.54, 0.09 for fermi level Ef = 0 eV and −1.31, −0.35, −0.94, −0.3 for P@C80, $S@C_{80}$, $As@C_{80}$, $Se@C_{80}$ at fermi level Ef = 0.1 eV. The remaining S and As-doped systems display significant drops in conductance in specific energy ranges. The conductance showed lower values in Fig. 5b, confirming the hypothesis that the material utilized for electrodes affected electronic transport. Moreover, the scattering effects at the molecule-graphene interface might explain why the conductance peaks are more pronounced. The conductance drift curves are consistent with the transmission spectra shown in Fig. 4, bolstering the hypothesis that charge transport properties are modified due to doping. Electrical conductivity values illustrated in Fig. 5b for $P@C_{80}$, $S@C_{80}$, $As@C_{80}$, and $Se@C_{80}$ are −1.98, −1.54, −3.34, and −1.26, respectively, at the Fermi level ($E_F = 0$ eV). For $P@C_{80}$, $S@C_{80}$, $As@C_{80}$, and $Se@C_{80}$, these values are −1.53, −1.23, −3.13, and −1.15, respectively, at the Fermi level ($E_F = 0.1$ eV).

Fig. 6 explains the thermoelectric properties of metalloid-doped C_{80} systems by graphing the Seebeck coefficient S against energy. For systems with gold (Au) electrodes is depicted in Fig. 6a, while Fig. 6b corresponds to electrodes made of graphene (Gr). Undoped C_{80} is tested as a reference, revealing the impact of P, S, As, and Se doping on thermopower, while considering both cases, the Seebeck coefficient has considerable dependence on energy and possesses numerous maxima and minima, highlighting the change of the dominating charge carrier type from electrons to holes [36]. The values for the Seebeck coefficient (S) presented in Fig. 6a are −13.74, −63.33, −8.27, and −28.28 mV/K for $P@C_{80}$, $S@C_{80}$, $As@C_{80}$, and $Se@C_{80}$, respectively, at the Fermi level $E_F = 0$ eV. All these values denote that the doped materials with Phosphorus, Sulfur, Arsenic, or Selenium exhibit a negative Seebeck coefficient at $E_F = 0$ eV, which is a characteristic of n-type behavior. The

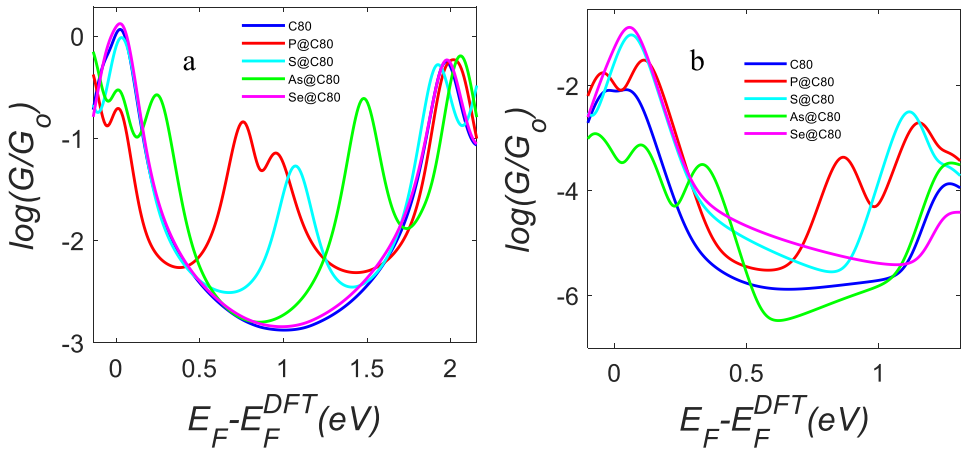

Fig. 5. The electrical conductance values log (G/G$_0$)for doped C_{80} systems with transition metals P, S, As, and Se as a function of energy ($E_F - E_F^{DFT}$) at room temperature.

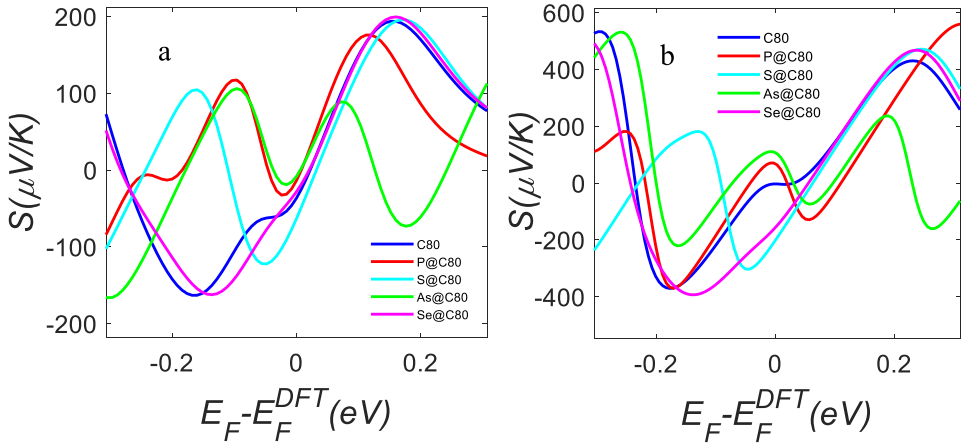

Fig. 6. The thermopower or Seebeck coefficient (S) as a function of energy ($E_F - E_F^{DFT}$) for P, S, As, and Se-doped fullerene cages C_{80} linked to (a) gold and (b) graphene electrodes.

values of the Seebeck coefficient (S) at $E_F = 0.1$ for P@C_{80}, S@C_{80}, As@C_{80}, Se@C_{80} are 169.97, 128.53, 63.55 and 147.86 mV/K respectively. This means that for all cases considered, when doped with Phosphorus or sulfur, arsenic, and selenium ions, the Seebeck coefficient is positive when $E_F = 0.1$ eV, signifying p-type formation. The C_{80} systems with metalloid dopants exhibiting a behavior change from n-type to p-type within the employed electric field are linked to the sophisticated phenomena involving the molecular orbitals of the doped fullerene and the electrode interacting with each other [37]. Doping modifies the charge carrier concentration and their type, and at the same time introduces localized states within the material, changing the electronic structure of the system around the Fermi level. Then at $E_F = 0$ eV, the Seebeck coefficient is negative, so transport is controlled by electrons because the dopant states are just under the conduction band, leading to n-type behavior. But, when the Fermi level is shifted to higher energy to $E_F = 0.1$ eV, transport becomes dominated by holes due to higher accessibility to levels that are above the Fermi level, leading to positive Seebeck coefficient and p-type behavior [38].

In comparison to the gold-based system, the graphene-based system generally achieves higher Seebeck coefficients, reasoning a thermoelectric advantage with graphene electrodes. The S and As-doped systems show marked peaks, indicating significant changes in thermopower because of the doping. The P-doped system shows a more damped shift while still keeping high values in both instances. The broader and higher peaks in Fig. 6b imply that gold electrodes provide a comparatively weaker thermoelectric response than graphene electrodes. Graphene electrodes seem to thermodynamically respond favorably during gold electrodes offered less responsiveness, as seen in Fig. 6b. Seebeck coefficient (S), was found to be 67.43, −201.81, 106.68 and −156.36 mV/K for P@C_{80}, S@C_{80}, As@C_{80}, Se@C_{80}, respectively, with the Fermi level $E_F = 0$ eV. It follows that with Phosphorus and arsenic ion doping, there's a positive Seebeck coefficient implying p-type. Doping with sulfur and selenium ions, however, indicates a negative means n-type formation. For the S@C80, As@C80 and Se@C_{80} the values are −32.33, 120.5, 8.67 and 139.86 mV/K while P@C80 are taken with $E_F = 0.1$. This suggests that S and S@C80 indeed point out that Phosphorus ion and Arsenic were doped, showing n-type resisting formation, while the other doped indicate a shift indicating p-type formation.

Fig. 7 shows the thermoelectric merit figure ZT as a function of energy for metalloid-doped C_{80} systems. Indicated in Fig. 7a are systems with gold (Au) electrodes, while Fig. 7b corresponds to electrodes made of graphene (Gr). The undoped C_{80} is used as a benchmark to analyze the impact of P, As, and Se doping on the thermoelectric performance. The variations in ZT value with energy are indicative of strong energy-dependent variation in thermoelectric efficiency. In Fig. 7a, maximum ZT values are lower than 2, even though the system with selenium doped shows the highest peaks. Fig. 7a shows that the values of the thermoelectric figure of merit are 0.01, 0.42, 0.003 and 0.06 for P@C_{80}, S@C_{80}, As@C_{80} and Se@C_{80} respectively at Fermi level $E_F = 0$. The values of figure of merit Ef = 0.1 eV equals 1.327, 1.325, 0.1 and 1.58 for for

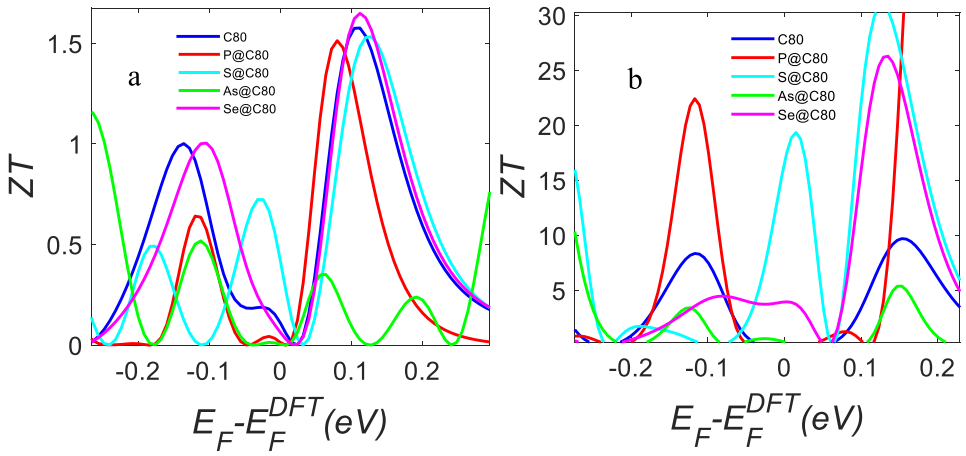

Fig. 7. The thermoelectric figure of merit ZT as a function of energy ($E - E_F^{DFT}$) for P, As, and Se-doped fullerene cages C_{80}, linked to gold (a) and graphene (b) electrodes.

P@C_{80}, S@C_{80}, As@C_{80} and Se@C_{80} respectively. In comparison, As-doped systems, particularly the As-doped system, surpass the value of 100 which is much greater than ZT values shown in Fig. 7b. This implies that the thermoelectric performance of graphene electrodes is significantly better than that of gold. Other peaks are also noted for the P-doped system which suggests other dopants affect thermoelectric efficiency through different means and ways. The selected regions of ZT with sharp peaks represent values where the processes of electronic transport, as well as the Seebeck coefficient, are at their zenith. These findings underscore more clearly the importance of dopant type as well as electrode material on the thermoelectric characteristics of C_{80} nanostructures, which is especially pronounced in systems with graphene electrodes where greater thermoelectric performance is expected. Fig. 7b displays the values of the thermoelectric figure of merit at the Ffermi level $E_F = 0$ are 0.13, 16.56, 0.32, 3.95 and for P@C_{80}, S@C_{80}, As@C_{80} and Se@$C_{80,}$ respectively. Whereas, for the stated values of the thermoelectric figure of merit at Ef = 0.1 eV, they are 0.44, 22.02, 0.03, and 15.91 for P@C_{80}, S@C_{80}, As@C_{80} and Se@$C_{80,}$ respectively.

The geometry of the molecular junction and the electrode arrangement have a significant impact on the augmentation of the thermoelectric figure of merit (ZT) in metalloid-doped C_{80} systems. Higher electrical conductivity (G) but lower Seebeck coefficients (S) because of weaker energy filtering are the results of the comparatively strong electronic interaction between the molecule and the metallic contacts when coupled to gold (Au) electrodes. Graphene (Gr) electrodes, on the other hand, frequently create sharper transmission characteristics due to their lower density of states around the Fermi level and weaker molecule–electrode interaction. This results in increased energy selectivity and greater S, even though G may be reduced. Furthermore, a lower total κ favors ZT enhancement due to graphene's lower inherent thermal conductance (κ) as compared to gold. Another important factor is the shape of the molecular junction: various metalloid dopants alter the energy alignment and spatial distribution of molecular orbitals, which causes the transmission peaks to move with respect to the Fermi level.

Fig. 8 shows the thermal conductance K as a function of temperature for the metalloid-doped C_{80} systems. Fig. 8a is for systems with gold (Au) electrodes, and Fig. 8b is for Gr electrodes. The undoped C80 is used as a reference to determine the impact of P, S, As and Se doping. In Fig. 8a, lower temperatures correspond to lower thermal conductance. However, at higher temperatures, the thermal conductance levels off. The Se-doped system has the highest thermal conductance, followed by the As and S doped systems. The P doped system demonstrates the strongest doped system demonstrates the strongest phonon scattering with the lowest thermal conductance. In figure 8a the value of electronic thermal conductance P@C_{80}, S@C_{80}, As@C_{80} and Se@$C_{80,}$are 6.33 × 10^{-11}, 1.77 × 10^{-10}, 1.21 × 10^{-10} and 3.63 × 10^{-10} respectively at T = 300K.

In Fig. 8b, the overall thermal conductance values are significantly lower than in Fig. 8a, suggesting that Gr electrodes reduce heat transport. The Se and P doped systems display higher values at intermediate temperatures, although the drift paths are distinct from those observed with gold electrodes. The reduction of thermal conductance in graphene-based systems is good for thermoelectric applications since it

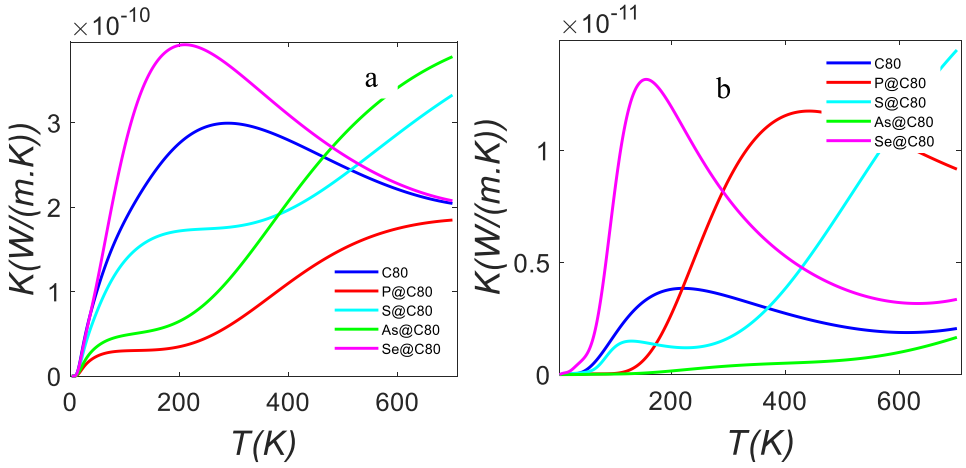

Fig. 8. The thermal conductance (K) as a function of temperature (T) for C_{80} doped with P, S, As, and Se, linked to gold (a) and graphene (b) electrodes.

improves the figure of merit ZT. For P@C_{80}, S@C_{80}, As@C_{80} and Se@C_{80}, the electronic thermal conductance values are 8.65×10^{-12}, 1.63×10^{-12}, 3.81×10^{-13} and 7.86×10^{-12}.

The observed reduced thermal conductance in the particular example of P@C_{80} is probably related to localized structural distortions brought about by the phosphorus dopant, which might interfere with vibrational modes that transmit heat.

3. Conclusion

This work is focused on the impact of metalloid doping and electrode modification on the electronic characteristics and thermoelectric properties of M@C_{80} molecular junctions. The transmission spectra support the fact that metalloid dopants form additional transport pathways which enhanced the delocalization of charges, modification the HOMO-LUMO gap. Thermoelectric efficiency assessed by the Seebeck coefficient and figure of merit showed that graphene-based junctions outperformed gold junctions. Especially, Se@C_{80} gave the highest ZT values, which improved the thermoelectric performance, reinforcing its use in thermoelectric devices. Also, the suggested thermal conduction deviations indicate that graphene electrodes maximize the energy conversion efficiency by restricting heat conduction. These results support the concepts related to charge transport in metallofullerene structures. They also provide new perspectives for the design of molecular electronics and advanced thermoelectric devices that perform optimally.

CRediT authorship contribution statement

Anhar A. Oda: Software, Investigation, Formal analysis. **Alaa A. Al-Jobory:** Writing – original draft, Supervision. **Sameer Nawaf:** Methodology, Investigation, Formal analysis. **Nabeel F. Lattoofi:** Writing – review & editing. **Moaaed Motlak:** Writing – review & editing. **Ali Ismael:** Resources.

Funding

The authors declare that no funds were received during the preparation of this manuscript.

Declaration of competing interest

The authors declare that they have no known competing financial interests or personal relationships that could have appeared to influence the work reported in this paper.

Appendix A. Supplementary data

Supplementary data to this article can be found online at https://doi.org/10.1016/j.mssp.2025.109822.

Data availability

The data supporting this study's results are available from the corresponding author upon reasonable request.

References

[1] C.G. Bischak, L.Q. Flagg, K. Yan, C.Z. Li, D.S. Ginger, Fullerene active layers for n-Type organic electrochemical transistors, ACS Appl. Mater. Interfaces 11 (2019) 28138–28144.
[2] Y. P Galvan, I. Alperovich, P. Zolotukhin, E. Prazdnova, M. Mazanko, A. Belanova, V. Chistyakov, Fullerenes as anti-aging antioxidants, Curr. Aging Sci. 10 (2017) 56–67.
[3] D.L. Wilson, J. Ahlawat, M. Narayan, The role of fullerenes in neurodegenerative disorders, J. Nanotheranostics 5 (2024) 1–12.
[4] S. Vidal, J. Marco-Martínez, S. Filippone, N. Martín, Fullerenes for catalysis: metallofullerenes in hydrogen transfer reactions, Chem. Commun. 53 (2017) 4842–4844.
[5] P. Fu, S. Zhou, Z. Liu, C. Wu, Y. Fang, Z. Wu, X. Tao, J. Yuan, Y. Wang, S. Gao, Multiprocessing quantum computing through hyperfine couplings in endohedral fullerene derivatives, Angew. Chem. 134 (2022) e202212939.
[6] S. Collavini, J.L. Delgado, Fullerenes: the stars of photovoltaics, Sustain. Energy Fuels 2 (2018) 2480–2493.
[7] A. Jaros, E.F. Bonab, M. Straka, C. Foroutan-Nejad, Fullerene-based switching molecular diodes controlled by oriented external electric fields, J. Am. Chem. Soc. 141 (2019) 19644–19654.
[8] D. Petrovic, M. Seke, B. Srdjenovic, A. Djordjevic, Applications of anti/prooxidant fullerenes in nanomedicine along with fullerenes influence on the immune system, J. Nanomater. 2015 (2015) 565638.
[9] S. Afreen, K. Muthoosamy, S. Manickam, U. Hashim, Functionalized fullerene (C60) as a potential nanomediator in the fabrication of highly sensitive biosensors, Biosens. Bioelectron. 63 (2015) 354–364.
[10] X. Lu, Z. Chen, Curved pi-conjugation, aromaticity, and the related chemistry of small fullerenes (< C60) and single-walled carbon nanotubes, Chem. Rev. 105 (2005) 3643–3696.
[11] H. Schmidt, F. Giustiniano, G. Eda, Electronic transport properties of transition metal dichalcogenide field-effect devices: surface and interface effects, Chem. Soc. Rev. 44 (2015) 7715–7736.
[12] M. Motlak, A. Hamza, S. Nawaf, Synthesis and application of Co/TiO2 nanoparticles incorporated carbon nanofibers for direct fuel cell, J. Phys. Conf. Ser. 1178 (2019).
[13] J.M. Hamill, A. Ismael, A. Al-Jobory, T.L.R. Bennett, M. Alshahrani, X. Wang, M. Akers-Douglas, L.A. Wilkinson, B.J. Robinson, N.J. Long, Quantum interference and contact effects in the thermoelectric performance of anthracene-based molecules, J. Phys. Chem. C 127 (2023) 7484–7491.
[14] F. Shafiq, L. Yang, W. Zhu, Computational studies on transition metal and nitrogen atoms co-doped fullerene as an efficient electrocatalyst for nitrate reduction to ammonia, Struct. Chem. 1–9 (2024).
[15] J. Sun, L. Ye, X. Zhao, P. Zhang, J. Yang, Electronic Modulation and Structural Engineering of Carbon-based Anodes for low-temperature lithium-ion Batteries: a Review Molecules, 2023, 28 2108.
[16] Q. Wang, J. Li, Y. Nie, F. Xu, Y. Yu, B. Wang, Pure spin current and phonon thermoelectric transport in a triangulene-based molecular junction, Phys. Chem. Chem. Phys. 20 (2018) 15736–15745.
[17] J. Yang, X. Yu, Z. Yu, L. Zhang, Spin thermoelectric transport of Co-salophene with borophene nanoribbon electrodes, Europhys. Lett. 135 (2021) 46001.
[18] S. Caliskan, A first principles study on spin resolved electronic properties of X@C70 (X= N, B) endohedral fullerene based molecular devices, Phys. E low-dimensional Syst. Nanostructures 108 (2019) 83–89.
[19] Oda A A and Al-Jobory A A 2025 effect of electrode type on electric and thermoelectric properties of M@ C60: M= P, As, and Se Int. J. Mod. Phys. B 2550140.
[20] M.H. Gafour, K. Saïl, G. Bassou, A. Haouzi, N. Maloufi, Theoretical Study of endohedral fullerenes M@ C 60 (M= Li, Na, or K) in periodic boundary conditions, J. Exp. Theor. Phys. 131 (2020) 548–557.
[21] S. Sarfaraz, M. Yar, K. Ayub, The electronic properties, stability and catalytic activity of metallofullerene (M@ C60) for robust hydrogen evolution reaction: DFT insights, Int. J. Hydrogen Energy 51 (2024) 206–221.
[22] D. Sergeyev, Single Electron Transistor Based on Endohedral Metallofullerenes Me@ C60, K, Me= Li, Na, 2020.
[23] S. Nawaf, J.M. Rzaij, A.A. Al-Jobory, M. Motlak, Investigating the optical properties and electronic structure of gallium phosphide nanotubes doped with arsenic via implementing first-principles calculations, J. Mol. Model. 30 (2024) 243.
[24] S. Nawaf, A.A. Al-Jobory, J.M. Rzaij, A.K. Ibrahim, First Principal Calculations on the Electronic Structure and the Optical Properties of Al-doped Zigzag Gan Nanotube Plasmonics 19 1–8, 2024.
[25] J.M. Soler, E. Artacho, J.D. Gale, A. García, J. Junquera, P. Ordejón, D. Sánchez-Portal, The SIESTA method for ab initio order-Nmaterials simulation, J. Phys. Condens. Matter 14 (2002) 2745.
[26] D.A. Ghafoor, W.M. Saod, N. Mohammed, Green synthesis of gold nanoparticles using pineapple extract and study their analytical characterization and antibacterial activity, Sys. Rev. Pharm. 11 (2020) 462–465.
[27] A.A. Khudhair, S.N. Mazhir, M.G. Hammed, Optical and structural characterization of Au@ ZnO core–shell nanoparticles prepared by pulsed laser ablation as anticancer agents for skin cancer, J. Opt. (2024) 1–10.
[28] K.A. Khalil, N.A.M. Barakat, M. Motlak, F.S. Al-Mubaddel, A novel graphene oxide-based ceramic composite as an efficient electrode for capacitive deionization, Sci. Rep. 10 (2020) 9676.
[29] M.S. Mahmoud, M. Motlak, N.A.M. Barakat, Facile synthesis and characterization of two dimensional SnO2-decorated graphene oxide as an effective counter electrode in the DSSC, Catalysts 9 (2019) 139.
[30] N.A.M. Barakat, M. Motlak, M.M. Nassar, M.A. Abdelkareem, M.S. Mahmoud, M. H. El-Newehy, H.M. Moustafa, From secondary to primary role in alkaline fuel cells: co-decorated graphene as effective catalyst for ethanol oxidation, ECS Electrochem. Lett. 4 (2015) F5.
[31] J. Ferrer, C.J. Lambert, V.M. García-Suárez, D.Z. Manrique, D. Visontai, L. Oroszlány, R. Rodríguez-Ferradás, I. Grace, S.W.D. Bailey, K. Gillemot, GOLLUM: a next-generation simulation tool for electron, thermal and spin transport, New J. Phys. 16 (2014) 93029.
[32] T. Lu, F. Chen, Multiwfn: a multifunctional wavefunction analyzer, J. Comput. Chem. 33 (2012) 580–592.
[33] T. Lu, A comprehensive electron wavefunction analysis toolbox for chemists, Multiwfn, J. Chem. Phys. 161 (2024).

[34] X. Wang, A. Ismael, S. Ning, H. Althobaiti, A. Al-Jobory, J. Girovsky, H.P.A. G. Astier, L.J. O'Driscoll, M.R. Bryce, C.J. Lambert, C.J.B. Ford, Electrostatic Fermi level tuning in large-scale self-assembled monolayers of oligo(phenylene-ethynylene) derivatives, Nanoscale Horizons 7 (2022) 1201–1209.
[35] M. Motlak, S. Nawaf, A.A. Al-Jobory, Investigation impact of (Ni, Cu) co-doping on the electronic, optical, magnetic, and I-V characteristics of GaP nanosheets *J. Mol. Model* 31 (2025).
[36] A.K. Ismael, I. Grace, C.J. Lambert, Increasing the Thermopower of crown-ether-bridged Anthraquinones, Nanoscale vol 7 (2015) 17338–17342.
[37] M. Alshammari, A.A. Al-Jobory, T. Alotaibi, C.J. Lambert, A. Ismael, Orientational control of molecular scale thermoelectricity, Nanoscale Adv. 4 (2022) 4635–4638.
[38] X. Wang, A. Ismael, B. Alanazi, A. Al-Jobory, J. Wang, C.J. Lambert, High Seebeck coefficient from isolated oligo-phenyl arrays on single layered graphene via stepwise assembly, J. Mater. Chem. C 11 (2023) 14652–14660.